JOURNAL OF CATALYSIS 103, 1–19 (1987)

The Mechanism of Formation of Ammonia Synthesis Catalyst

G. M. PENNOCK,* H. M. FLOWER,† AND S. P. S. ANDREW‡

*Pye Unicam Ltd., Cambridge, England; †Department of Metallurgy and Materials Science, Imperial College, London, England; and ‡ICI PLC Agricultural Division, Billingham, Cleveland, England

Received March 18, 1985; revised March 24, 1986

The formation of ammonia synthesis catalyst by the reduction of magnetite by hydrogen at 450°C has been studied using electron microscopy, X-ray energy dispersive and electron energy loss analysis, and including *in situ* reduction experiments in a gas reaction cell in an electron microscope. The reaction is characterised by a cellular mechanism of reduction leading to the formation of a periodic network of iron crystallites and pores without any significant volume change. The iron nucleates epitaxially on the oxide, and minor elements, notably aluminium, initially in solution in the oxide, partition to the iron crystallite surfaces. Elements present in intercrystalline ferrite and glassy phases remain essentially immobile during reduction with the exception of potassium which migrates rapidly to the iron surfaces.

INTRODUCTION

The ammonia synthesis catalyst is an example of a wide range of industrially important, heterogeneous catalysts that have a high specific metal surface area formed by the partial reduction of a metal oxide/refractory oxide solid solution or compound. In the commercial material the catalyst is produced by reduction of magnetite, Fe_3O_4, to metallic iron using a H_2/N_2 atmosphere at approximately 450°C, i.e., below the wüstite/magnetite transition temperature. The addition of nitrogen permits the formation of ammonia as the magnetite is reduced and the exothermic reaction of the ammonia synthesis partially compensates for the endothermic reduction reaction.

Small quantities of selected oxides of Si, Al, K, and Ca and traces of Ti, V, and Zr oxides are fused with the magnetite at approximately 1600°C prior to reduction (*1*, *2*). A small amount of the Al, Ca, and Mg form a substitutional solid solution in the spinel magnetite lattice, the excess forming intergranular orthorhombic ferrite phases (*3–7*), the objective being to promote the formation of potassium ferrite (*1*). Excess Al and Si also react with Ca and K to form intergranular glassy aluminosilicates (*1*, *3*). The reduction transformation occurs without shrinkage and thus the removal of oxygen gives rise to a highly porous structure. X-Ray line broadening, transmission electron micrographs of replicas and scanning electron microscopy of bulk samples show that the iron is in the form of small crystallites, less than 40 nm in diameter (*1*, *8*, *9*). A stable form of the reduced magnetite, referred to as the prereduced catalyst, is commercially obtained by partial reoxidation of the porous iron in a controlled atmosphere of O_2/N_2.

The oxide additions, or promoters, are generally classified as being either structural or chemical depending on their primary function. Structural promoters are added to produce a high, stable surface area of catalyst whereas chemical promoters improve the activity of the catalyst. Structural promoters are refractory oxides, e.g., Al_2O_3, and chemical promoters are alkali metal oxides, e.g., K_2O. The location of the promoters in the reduced granules is of prime importance to the catalytic efficiency. Various techniques, including gas adsorption, line broadening in X-ray diffraction, Mössbauer, scanning Auger electron, and X-ray photoelectron spectroscopy have been used to elucidate the

0021-9517/87 $3.00

chemical constitution of the iron surface (*8–12*). Chemisorption of CO_2 gas has shown that potassium in the ferrite phase (*1*) redistributes itself throughout the iron during reduction and is concentrated on the surface of the iron crystallites as would be expected from its effect on the activity (*2, 10*). Optimum catalytic activity is obtained when 25–30% of the iron surface is covered with potassium. Estimates from the chemisorption of CO suggest that the free iron surface is quite small, ~10–30% of the total area (*1*). It is assumed that the remaining surfaces of the iron crystallites are covered with refractory oxide promoters which precipitate out of solution as the magnetite matrix is reduced, thus hindering sintering between the crystallites. There is some controversy as to the nature of the alumina complex within and around the iron crystallites (*2, 8, 9, 11–13*).

The reduction reaction has been described by a "core and shell" model in a dry atmosphere and a "crackling core" model in the presence of moisture (*14–16*). In the former case the iron forms a continuous shell around a core of oxide with a well developed reaction interface. In the latter reduction occurs at sites throughout the oxide. This form of reduction is also promoted by the presence of wüstite in the magnetite: cracks or large pores are assumed to develop as reduction proceeds leading to gas access to the grain interiors (*15*) but slower reaction kinetics (*14*). In all cases the reduction reaction leads to the formation of microporous iron and it is interesting to note that the pore size is substantially larger in iron produced by wüstite reduction (*16*) than that produced by magnetite reduction.

Baranski *et al.* (*14*) have modelled the core and shell reduction assuming gas transport control, but allowing for adsorption of water, and mixed reaction control, including solid state transport processes, has also been cited (*17*). Additionally the influence and the distribution of minor oxide additions on the reduction reaction and the microstructure developed is uncertain. The understanding of these details is of technical interest and could lead to improved catalyst formulations for a wide range of heterogeneous catalysts. The objective of the present work has been to elucidate some of these details by duplicating the conditions of reduction in the catalytic reactor in a gas reaction cell of a high voltage electron microscope.

EXPERIMENTAL

The experiments have been conducted in the gas reaction cell of a high voltage electron microscope (*18, 19*), thus permitting direct observation of the reduction mechanism. Further characterization of the microstructure and microchemistry in the unreduced magnetite and prereduced catalyst was investigated using transmission and scanning electron microscopy together with X-ray energy dispersive spectroscopy (EDS) and electron energy loss spectroscopy (EELS). Prereduced granules were vacuum impregnated with an Araldite resin prior to ion beam thinning for transmission electron microscopy.

RESULTS

Characterization of the Catalyst Precursor

Examination of the catalyst precursor (unreduced magnetite) prior to reduction confirmed the previous work with regard to the form and distribution of the minor element additions: small quantities of Ca and Al and occasionally K were contained in solid solution in the magnetite matrix (Table 1), the excess oxide additions forming intergranular ferrites and aluminosilicate phases. Additionally the magnetite matrix was found to contain clusters of faults on {111} planes (Fig. 1). Limited EDS analysis suggests that the more faulted regions contain a higher concentration of Ca and/or K.

TABLE 1

X-Ray Energy Dispersive Analyses from Reduced and Unreduced Matrix Regions in a Bulk Sample of a Partially Reduced Granule

Element[a]	ZAF[b]	Magnetite (unreduced) (wt%)			α-Iron (reduced) (wt%)		
Mg	0.29	0.3[c]	0.9	0.3[c]	0.1[c]	0.8	0.3[c]
Al	0.40	2.0	2.2	2.4	1.9	2.1	2.0
Si	0.54	0.3	0.0[c]	0.1[c]	0.0[c]	0.1[c]	0.1[c]
Ti	1.08	0.1[c]	0.0[c]	0.0[c]	0.0[c]	0.0[c]	0.0[c]
K	0.99	0.5	0.1[c]	0.0[c]	1.6	1.5	1.7
Ca	1.15	0.5	0.4	0.5	0.5	0.6	0.5
V	1.10	0.0[c]	0.0[c]	0.1[c]	0.0[c]	0.0[c]	0.1[c]
Cr	1.27	0.0[c]	0.0[c]	0.0[c]	0.0[c]	0.1[c]	0.0[c]
Mn	0.97	0.2[c]	0.2[c]	0.1[c]	0.0[c]	0.0[c]	0.0[c]
Fe	0.99	96.1	96.2	96.5	95.9	94.8	95.3
Fit index		1.48	1.88	1.23	1.07	1.99	1.31

Note. All concentrations are normalised to 100% excluding oxygen.

[a] K-1 edge used in analyses.

[b] Average ZAF correction quoted: the values were the same to two decimal places in analyses.

[c] Concentrations of these elements were too small to be statistically significant.

Characterization of the Prereduced Material

Light microscopy of polished sections of the prereduced catalyst showed that the parent magnetite grains contain a high density of predominantly crystallographically oriented channels (Fig. 2). Higher resolution back scattered electron imaging of these regions using SEM showed that the channels which emanate from the grain boundaries are wider in the vicinity of the grain boundary and tend to form along traces parallel to the parent magnetite ferrite interfaces (Fig. 3). The changes in contrast using back-scattered electron imaging not only reflect the differences in composition between the various phases in the reduced material (Fig. 3a) but also differences in the density of the reflecting surface; thus the channels appear as dark lines. The

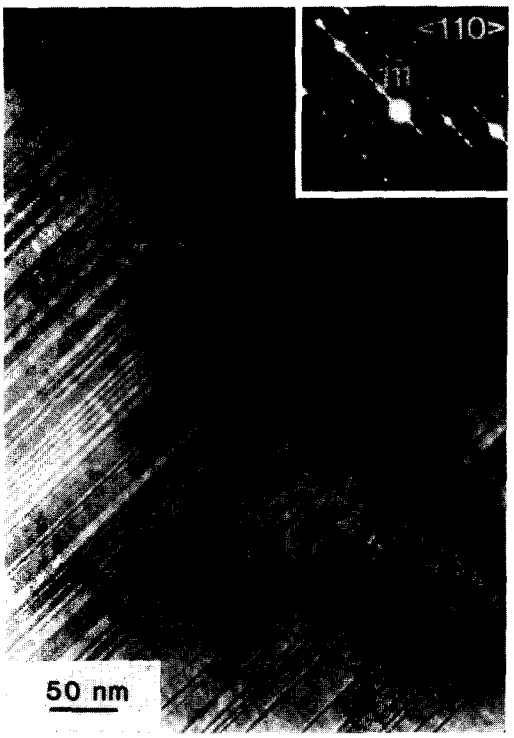

FIG. 1. Transmission electron micrograph of a finely faulted region of magnetite and the corresponding diffraction pattern (inset) showing extensive faulting on {111} planes.

FIG. 2. Light micrograph of a polished section of a prereduced granule showing the extent of the reduction reaction. The parent magnetite grains contain a high density of crystallographically oriented channels.

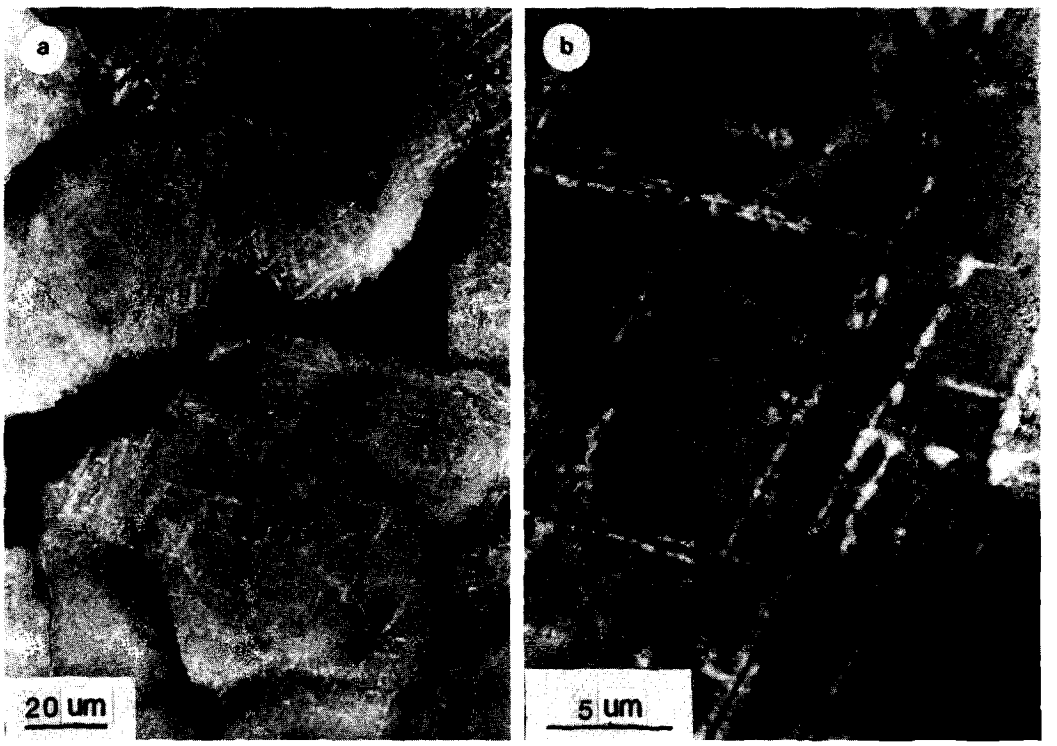

FIG. 3. Back-scattered electron image of a polished section of a prereduced granule illustrating (a) the compositional differences between the intergranular ferrite regions (dark areas) and the iron matrix and (b) the crystallographic nature of the channels penetrating the iron matrix, and the difference in density within this region.

"speckled" appearance of the regions between the channels suggests a very fine scale porosity, and the whiter contrast surrounding the channels, less porosity (Fig. 3b).

Further microstructural details of the reduction induced transformation were obtained by breaking open the prereduced granules and examining the fracture surfaces using the secondary electron imaging mode. Fracture of the granules occurred quite easily along both inter- and transgranular paths (Fig. 4a) reflecting weaknesses in the microstructure caused by the heterogeneous distribution of phases at grain boundaries and by the channels which penetrate the grain interiors. Figure 4b illustrates the crystallographic nature of the channels and also demonstrates that the regions between the channels are porous, which is seen more clearly at higher magnifications (Fig. 4d).

It can be seen that the channel planes intersect the fracture surface at 60°. If it is assumed that transgranular fracture occurs on {111} planes, in agreement with general observations in fcc systems, then it can be deduced that the channels also form on the close packed {111} planes (the traces of {111} planes alone intersect at 60° in a ⟨111⟩ projection). It is probable that the channels grow in the ⟨110⟩ close packed directions of the parent oxide.

Transmission electron microscopy of impregnated thin foils confirmed the observations on bulk material, and provided the means to study in detail the characteristics of the reduction product. Figure 5a is a low magnification composite micrograph in which the crystallographic orientation of

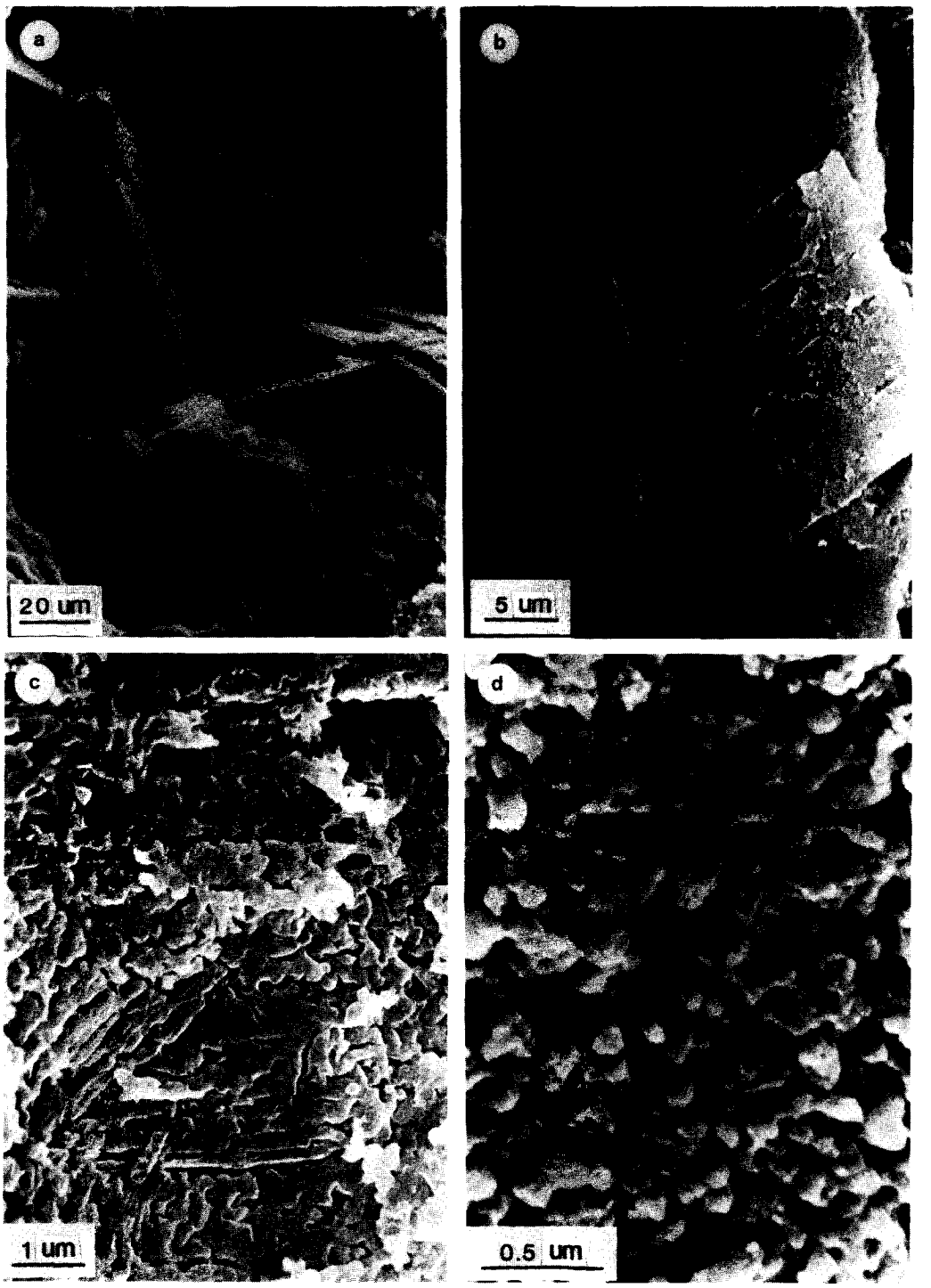

FIG. 4. Secondary electron SEM micrographs showing the topography of a fractured surface of prereduced material (a) at low magnification, where predominantly intergranular fracture has occurred along crystallographically orientated channels, (b) where a network of finer, crystallographically orientated channels is seen to penetrate the grain centre at intermediate magnification, (c) which shows a fine-scale interlocking network of porosity, and (d) which shows the extensive porosity of the reduction product, namely the small α-Fe crystallites.

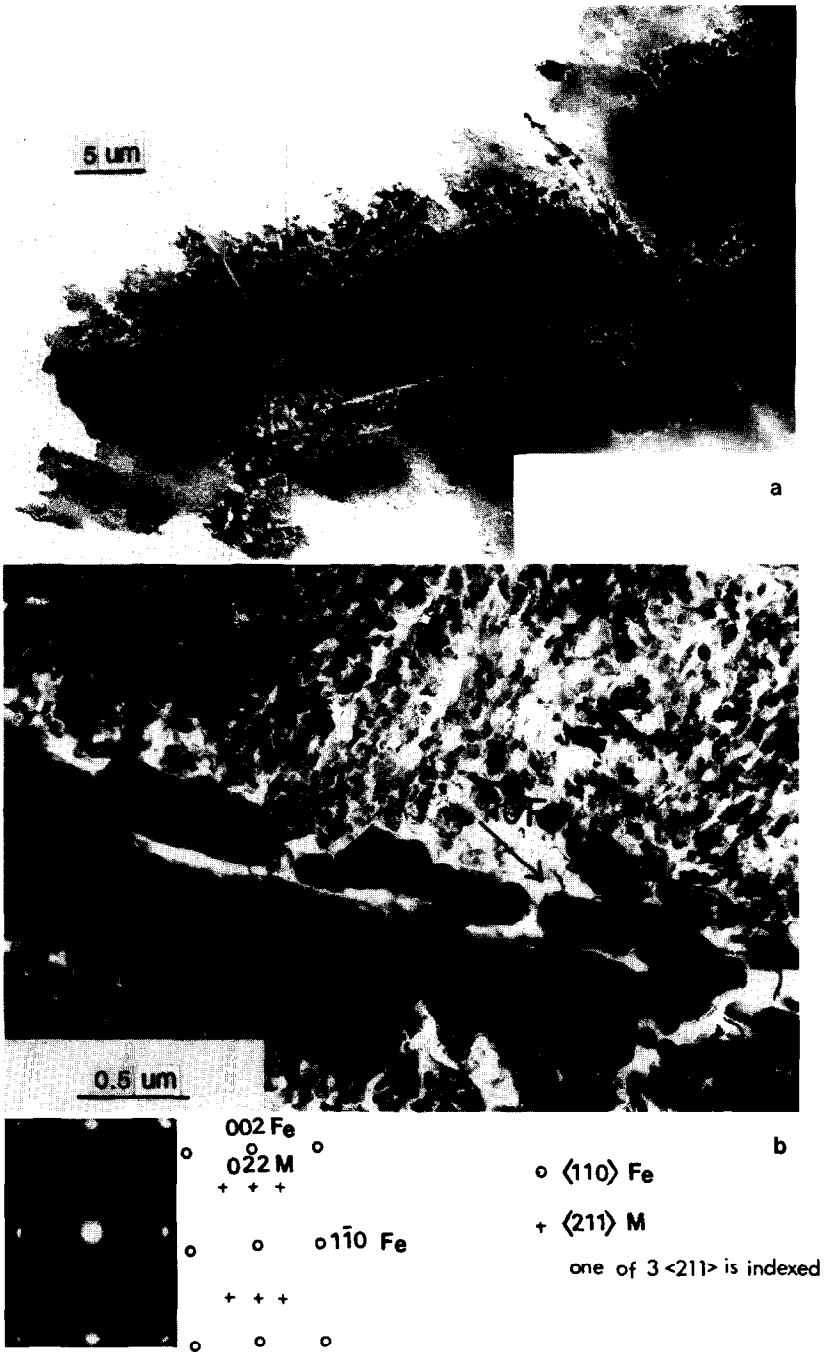

FIG. 5. (a) Composite transmission electron micrograph of a large area of electron-transparent prereduced and impregnated catalyst showing large, crystallographically orientated channels (b) at higher magnification showing the larger, sintered crystals lining the channel and the fine, microporous region containing small crystallites of α-iron. The corresponding diffraction pattern shows that the crystallites are all in the same orientation and contains weak orientated diffraction maxima from the magnetite phase, caused by partial reoxidation. The key to the diffraction pattern is also given.

the channels is clearly evident. It is also apparent that the bulk of the reduced material is comprised of small, faceted crystallites, ~50 nm in size. An extremely fine network of micropores, as small as 5 nm in diameter, form boundaries between the crystallites (Fig. 5b). The crystals lining the channels are considerably larger than those in the microporous region and appear to consist of several sintered crystallites. This confirms the interpretation given earlier to observations made on back-scattered electron micrographs of polished, bulk samples (Fig. 3b).

Analysis of electron diffraction patterns established that the crystallites were α-iron. In some regions the α-iron crystallites exhibited single crystal diffraction patterns (Fig. 5b), whereas in other regions the α-iron crystallites were more randomly orientated. It was found that the randomly orientated crystallites were larger (~100–300 nm compared to ~30–100 nm), more widely spaced and comprised of sintered or overlapping crystallites. It is probable that these regions originate from sections of foil made parallel to the channel planes, and through the larger crystals that line them. Diffraction patterns taken from the microporous regions on either side of various channels were shown to have the same orientation, indicating that the channels had grown through a grain of magnetite, and not along a grain boundary, which would be expected to have a high angle of misorientation.

Selected area and microbeam diffraction patterns of individual crystallites both contained diffuse diffraction maxima from an orientated second phase (see Fig. 5b). These weaker diffraction maxima also exhibited cubic symmetry, and analysis established that the interplanar spacings were compatible with the magnetite phase. This observation is consistent with chemisorption measurements which have shown that ~30% of the reduced iron surface is reoxidized during stabilization of the granules (9). The orientation relationship between the magnetite and α-iron phases was established as

⟨100⟩ fcc ‖	⟨011⟩ bcc
Magnetite	α-Fe
{001} fcc ‖	{100} bcc

High resolution dark field image analysis established that the magnetite phase was located on the peripheries of the α-iron crystallites (Fig. 6) in the form of discrete particles 15–30 Å in size. The layer is continuous, and consistency with chemisorption information requires that other phases apart from the reoxidation product of magnetite are also present.

High resolution X-ray energy dispersive and electron energy loss spectroscopy (EELS) were used to provide further information concerning the chemistry of the layer surrounding the α-iron crystallites. This work was carried out using a Philips 400T instrument with EDAX analytical attachments and a Gatan EELS. The microscope was operated at 100 kV with a beam current typically 100 μA: the spot size was adjusted for analysis to a size down to ~2 nm. X-Ray energy dispersive analysis showed that the centres of the α-iron crystallites were iron-rich, with only traces of aluminium and calcium, whereas the surface layer was rich in the lighter elements, magnesium, aluminium, potassium, and calcium. The distribution of these phases was highly heterogeneous. A typical X-ray spectrum showing an aluminium-rich region is shown compared with a grain interior region in Fig. 7. X-Ray spectra obtained from small diffracting regions embedded in the resin were also found to be rich in the lighter elements. Electron energy loss spectroscopy (Fig. 8) confirmed the X-ray energy dispersive observations, and established the presence of significant amounts of oxygen in the thin layer. Similar analysis of a grain interior contained only a trace of oxygen which may be assumed to be present as a very thin superficial layer on the foil surface.

In certain regions, the fine-scale distribution of the α-iron crystallites and pores was

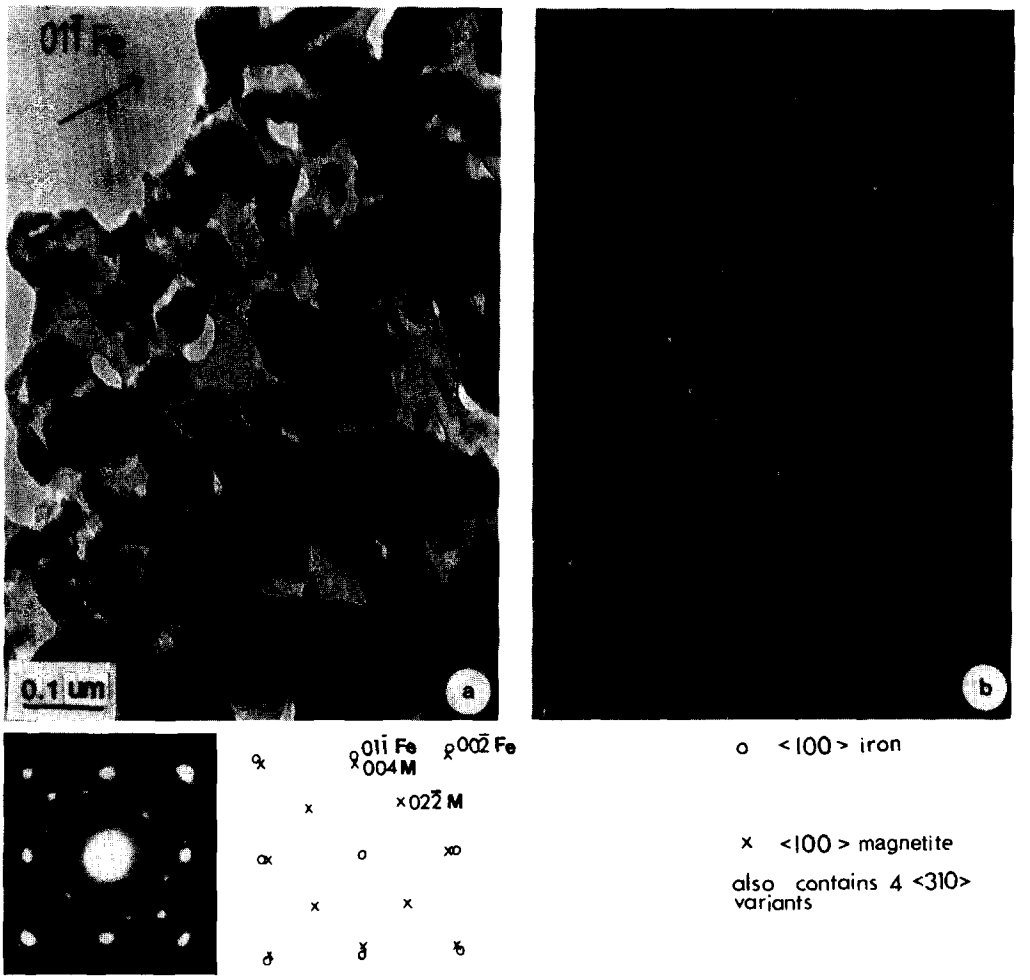

FIG. 6. (a) Bright field and (b) dark field ($g = 02\bar{2}$ magnetite) images, showing the magnetite phase located on the surfaces of the iron particles. The corresponding diffraction pattern and key are also given.

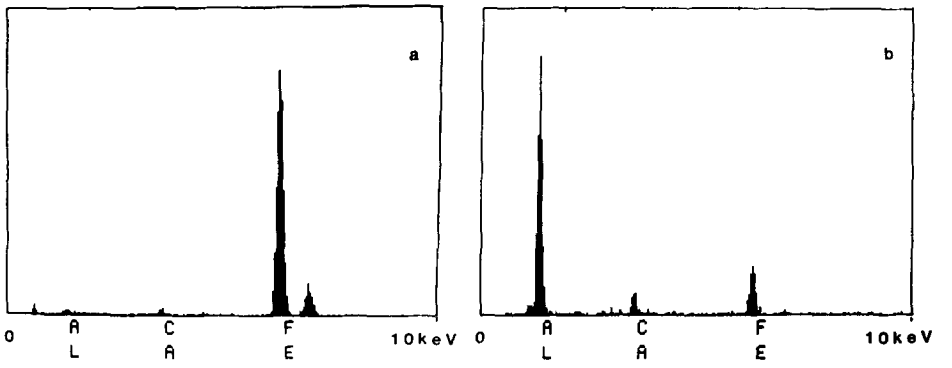

FIG. 7. X-Ray energy dispersive analysis of a thin foil of prereduced material (a) from the centre and (b) from the edge regions of an α-iron crystallite, showing a higher proportion of the lighter elements in the edge region (count rate 1500 cps, lifetime 100 s).

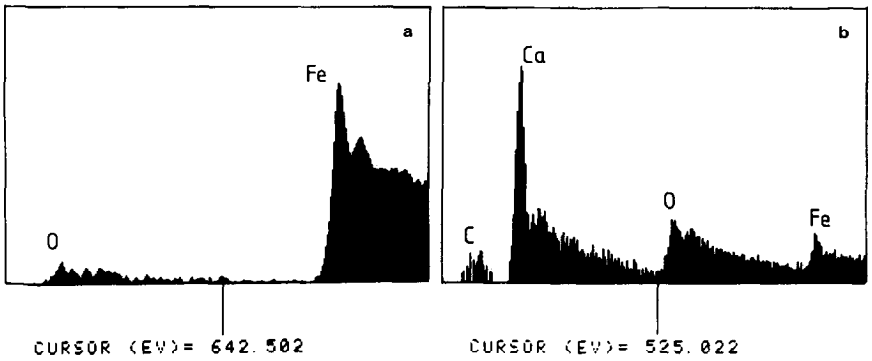

FIG. 8. Electron energy loss spectra from a thin foil of prereduced material, confirming that a higher proportion of the lighter elements and oxygen are contained in the edge regions of the iron crystallites.

interpenetrated by long, thin crystallites and platelets (Fig. 9). The concentration of Al, K, and Ca was considerably higher in the longer crystals than in the fine-scale porous iron (Fig. 10). The concentration of K and Ca in the larger, blocky crystallites was perhaps marginally greater than in the very fine porous regions of iron. Microbeam electron diffraction techniques of thin sections using TEM showed that adjacent long crystals were alternatively in a ⟨100⟩ or ⟨111⟩ cubic zone (Fig. 11).

Partial Reduction of Bulk Material

Polished metallographic sections of laboratory-reduced granules showed that only a narrow region of material had undergone reduction after 26 h. The reduced region was evident as a uniformly thick, lighter grey region, which was visible to the unaided eye. The characteristics of the reduced region in the bulk sample were essentially the same as observed in sections of commercially reduced material, viz., the reduced grains contain crystallographically orientated channels, which lay parallel to the ferrite/matrix interface.

Channels are also observed in the ferrite phase. Figure 12 shows details of a region across the reaction interface. It can be seen that the reduction reaction proceeds more rapidly along grain boundaries and along the channels which emanate from the ferrite regions into the bulk of the grain; thus "islands" of unreduced magnetite are created in the α-iron grains.

X-Ray images taken in the form of a 128 × 128 matrix of spot analyses across the reaction interface indicated that of the minor elements initially concentrated in the intergranular phases only potassium migrated during reduction and became homogeneously (that is, within the 3-μm limit of resolution of the analysis technique) distributed throughout the reduction product (Fig. 13). Table 1 presents the quantitative analysis from regions of α-iron and magnetite in reduced and unreduced regions, respectively. It is clear that the concentration of potassium has increased dramatically in the reduced regions of α-iron.

HVEM in Situ Reduction of Thin Foil Material

Characterization of the mechanism of the reduction transformation using the environmental cell of the HVEM was successfully carried out. Examination of the microchemistry before and after reduction was, however, difficult to achieve, primarily because the thin film disks were exceptionally friable, especially after reduction, owing to the preferential removal of the intergranular phases during ion beam thinning and the physical nature of the reduction products. The results presented below summarize the salient features of the reduction sequences

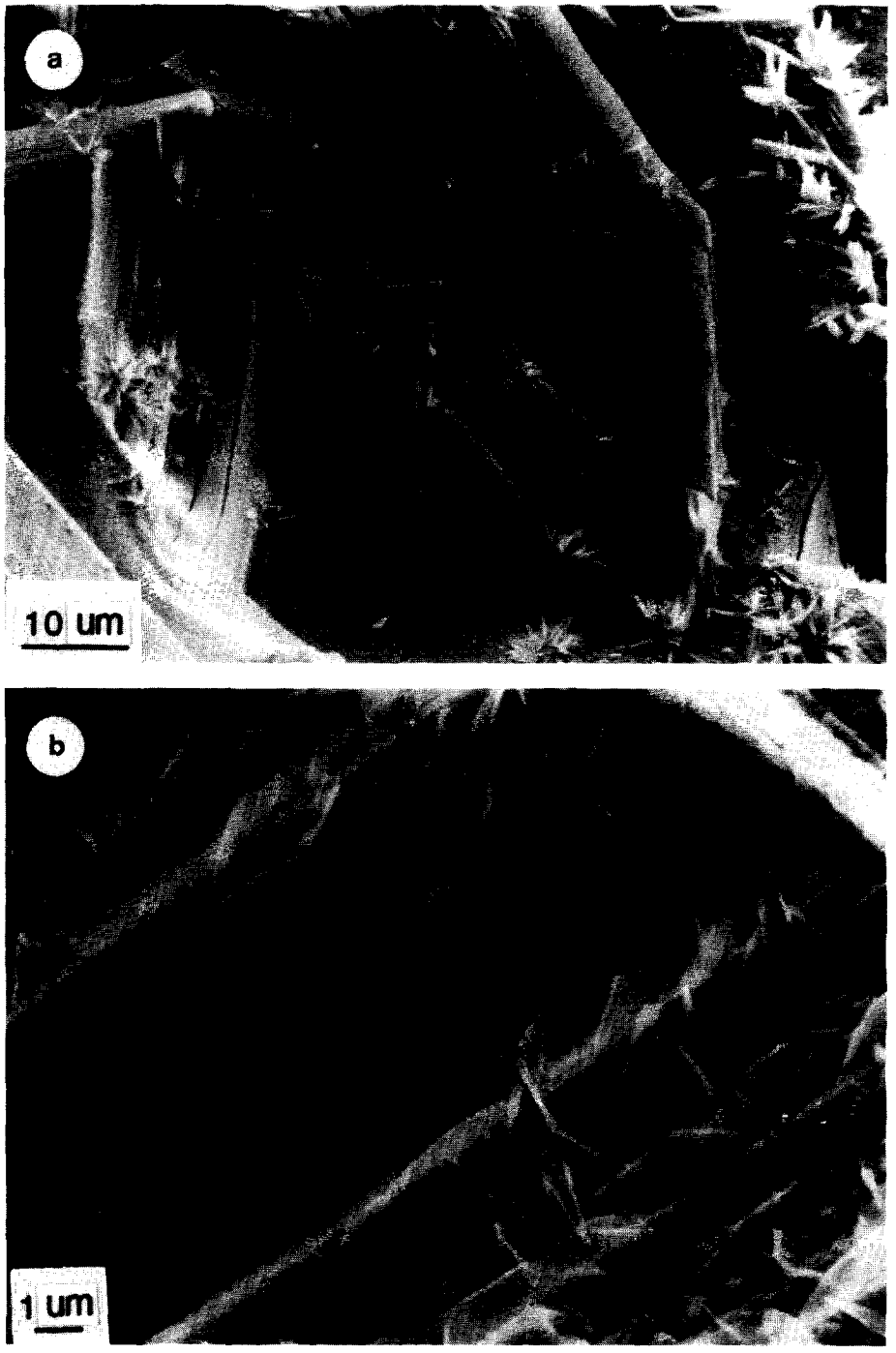

FIG. 9. Secondary electron SEM micrographs of a fractured surface of a prereduced granule showing regions containing long, thin crystals. (a) Shows clusters of needles, larger, long plates, and some blocky crystals. (b) Shows very thin interpenetrating platelets in the fine porous α-iron. Some more blocky α-Fe crystals are also present.

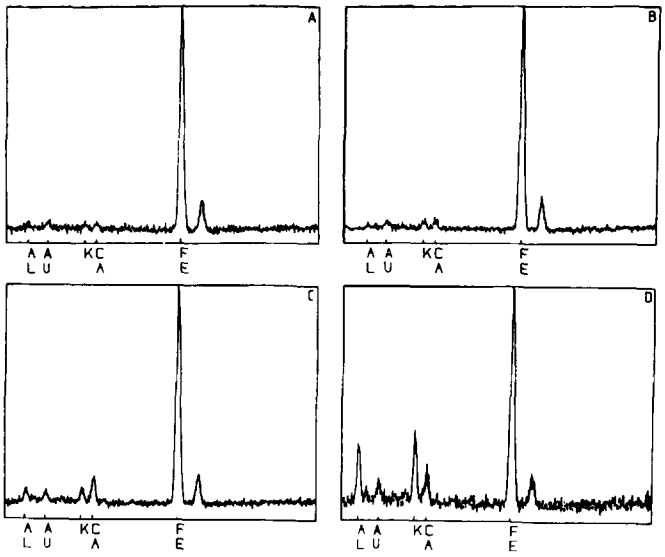

FIG. 10. Energy dispersive X-ray spectra from the fracture surface of a prereduced granule, typical of regions containing (A) small α-Fe crystallites (shown in Fig. 4d), (B) larger, blocky crystallites (shown in Fig. 9), (C) thin platelets and radially distributed long, thin, crystals (shown in Fig. 9), and (D) large long crystals, presumably ferrites, containing a high concentration of aluminium and calcium (shown in the right-hand side of Fig. 9a). These samples were gold coated.

observed in the magnetite matrix during *in situ* reduction.

The sequence of micrographs in Fig. 14 illustrate the mechanism of the reduction reaction. The transformation was carried out at 450°C in 20 Torr of 10% hydrogen/nitrogen gas. The sequence shown was taken after 2200 s in a region adjacent to a

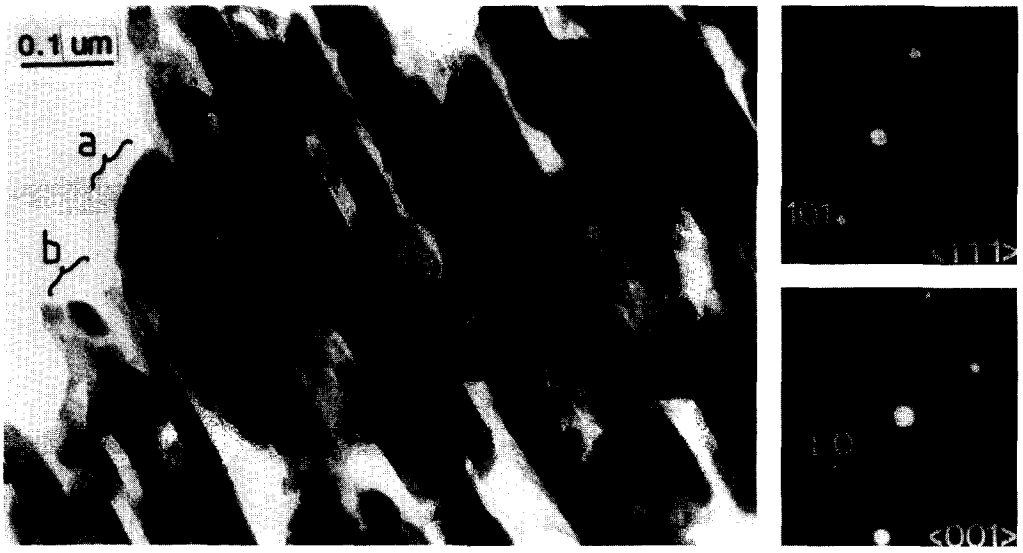

FIG. 11. Bright field transmission electron micrograph of prereduced material showing long crystals, which interpenetrated more blocky crystals of α-iron. Also shown are the microbeam diffraction patterns from adjacent long crystal regions; region *a* exhibited a ⟨100⟩ zone axis and region *b*, a ⟨111⟩ zone axis.

FIG. 12. Light micrograph of partially reduced granule showing the reaction interface. The light grey region is α-iron and the darker grey region is the unreduced magnetite. The arrowed region shows rapid reduction along crystallographically orientated channels into the magnetite.

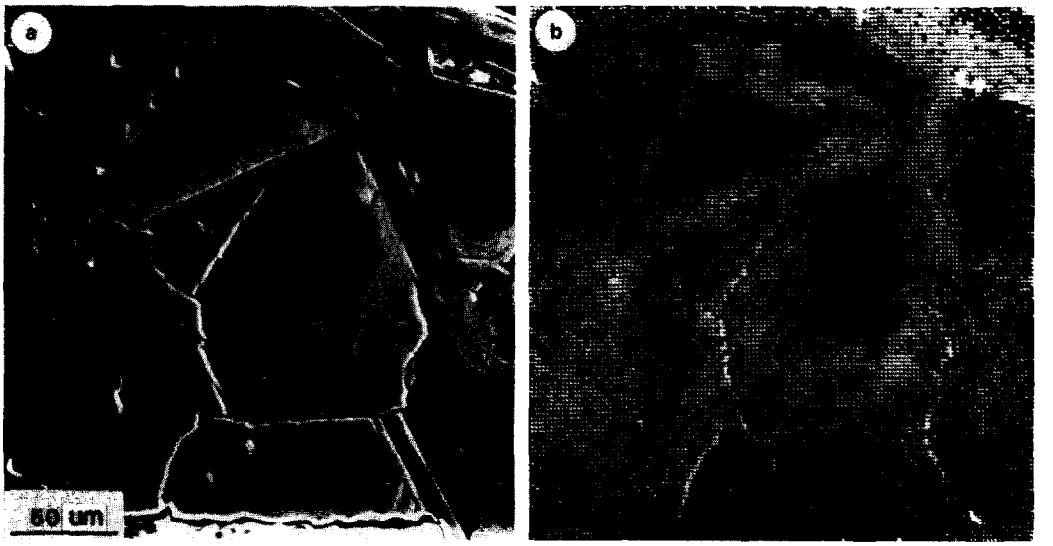

FIG. 13. (a) Secondary electron SEM micrograph of the edge of a partially reduced granule showing the iron–magnetite interface and (b) the corresponding potassium digital X-ray map showing that extensive migration has occurred from intergranular regions becoming uniformly distributed throughout the reduction product.

fine grain sized region. (A reduction transformation resulting in extensive porosity had already occurred in and around similar regions in other thin areas of the foil.) The reduction reaction proceeded by a mechanism analogous to cellular decomposition, thus producing a periodic structure of iron and pores. This process permits reduction to occur without any external change of shape or shrinkage, in agreement with observations made on bulk material.

Selected area diffraction from the area before the start of the transformation (Fig. 14) shows diffraction maxima from the magnetite phase; the other diffraction maxima arise from the strongly diffracting small grain, which is probably a ferrite grain. Diffraction across the reaction interface (Fig. 14) confirms the presence of two variants of the α-iron phase in the reduced matrix. The orientation relationship between the magnetite (M) and α-iron (Fe) is found to be

$$\langle 311\rangle \text{ Fe} \sim \| \langle 120\rangle \text{ M}$$
$$\{100\} \text{ Fe} \sim \| \{100\} \text{ M}$$

which is a variant of the relationship given above for the α-iron–magnetite phases in the prereduced material.

The reaction proceeds predominantly along crystallographic directions. No more than four variants are observed which is consistent with growth on {111} planes in the magnetite. The pores and crystallites are approximately 20–30 nm in diameter. An estimation of the reduction front migration rate along one of the dominant growth directions was determined from Figs. 14c and d using the ferrite grain as a reference marker, giving a value of 2×10^{-9} m s^{-1}. Similar periodic microstructures were observed after *in situ* reduction in other thin foil areas located close to grain boundaries or surrounding a hole, presumably in regions where ion beam thinning had removed the majority of the glassy or ferrite phases.

Details of the reduction reaction in other regions of the unreduced catalyst will now be described. The main characteristics of the reduction transformation observed in faulted ferrite and magnetite regions were similar. A mottling and/or rumpling of the thin foil marks the start of the transformation, the rumpling occurring parallel to the faults. This reaction occurs quite rapidly, within ~300 s, where $t = 0$ defines the time when the furnace temperature was raised from 50 to 450°C, which took ~100 s. As the microstructure coarsens the stacking fault contrast across the fault planes is lost, and a fine-scale porosity becomes apparent. The pores show a preference to form at the intersection of the faults with the foil surface (Fig. 15). Channels form along the fault traces as the pores coarsen and coalesce, and a fine precipitation reaction occurs; the growth of the precipitates is enhanced by the beam, and the whole transformation occurs more rapidly in the thinner regions at the foil edges and in regions adjacent to the glassy phases.

DISCUSSION

The Unreduced Material

TEM has shown that the unreduced magnetite lattice is highly faulted on {111} planes (Fig. 1), which is the close-packed plane for oxygen ions in the magnetite lattice (*5*). Microchemical analyses (Table 1) have confirmed that small quantities of aluminium and calcium form substitutional solid solutions with the magnetite lattice in agreement with the literature (*3, 4, 7*). Qualitative analyses of thin foils showed that the concentrations of calcium in the magnetite lattice varied. Regions that were high in calcium were either highly faulted or formed very small grains. It is suggested that the larger ionic radius of the Ca^{2+} ion and orthorhombic structure of $CaFe_2O_4$ limits the solubility of this ion in the magnetite lattice. Faulting on {111} planes locally creates a region of hexagonal stacking closely related to that in the orthorhombic ferrites. There was also some evidence to show that

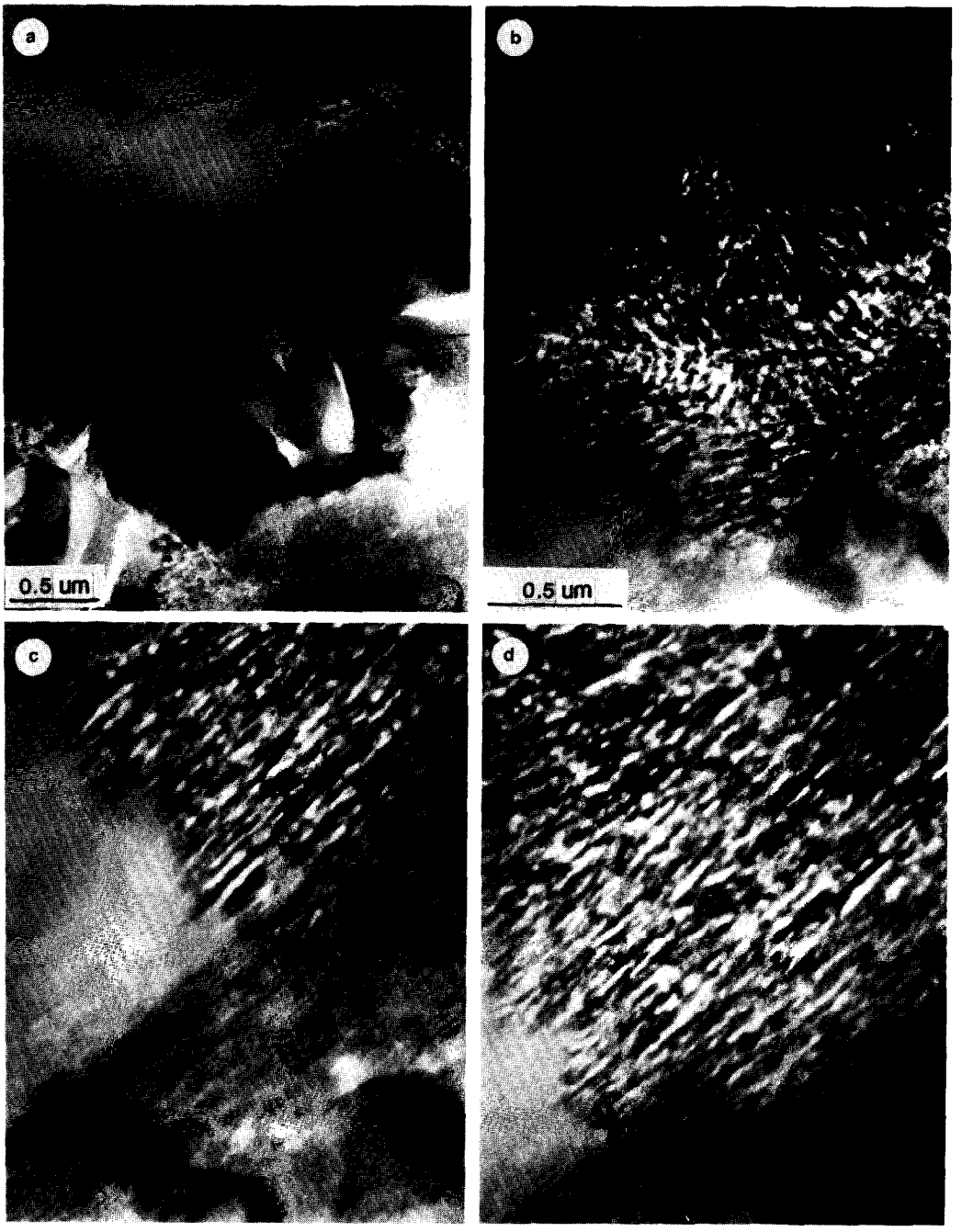

FIG. 14. HVEM *in situ* reduction sequence of magnetite in a region adjacent to small ferrite grains showing the development of a periodic microstructure of small iron crystallites and pores. (a) Low magnification showing the location of the initial transformation, (b) a slightly higher magnification showing rapid growth of four variants of α-iron. Transformation after (c) 3086 s and (d) 3155 s showing preferential growth of one variant. Diffraction patterns taken after (e) 2176 s, just before the start of the transformation, and (f) across the growing reduction interface.

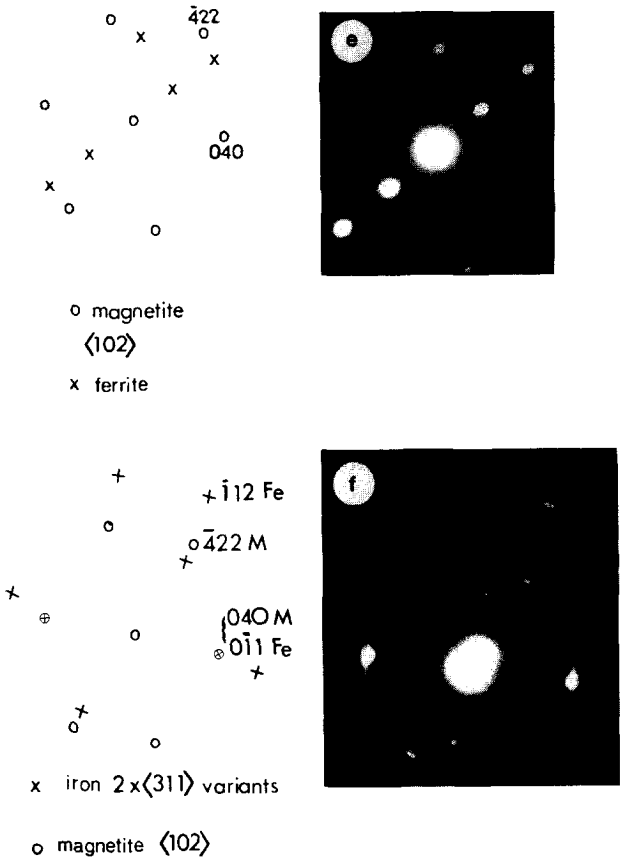

FIG. 14—*Continued.*

these regions were adjacent to grain boundaries and ferrite phases. Such concentration gradients are to be expected in the as cast magnetite grains. Potassium was generally not detected in the magnetite lattice, in agreement with other work (*3, 4, 7*), although occasionally small concentrations were detected in both thin foil and bulk analyses. Small quantities of orthorhombic $KFeO_2$ are reported to be soluble in magnetite (*2*). TEM showed that the magnetite regions containing potassium also contained high concentrations of calcium.

Thin foil *in situ* experiments have shown that pore development occurs more rapidly along fault planes (Fig. 15). The microstructure in partially reduced material also implies that the reduction transformation occurs more rapidly along fault planes in the calcium-enriched magnetite regions (Fig. 12). Trace analysis of the channel planes in fracture surfaces confirms that channels form along the {111} fault planes observed in unreduced material. Thus the larger channels that are observed in the prereduced microstructure (Fig. 5) are thought to originate from rapid reduction along the fault planes caused by refractory oxide additions which exhibit limited solubility in the magnetite lattice, notably calcium. It is of interest to note that the iron crystallites in these regions are larger as a result of sintering.

It is quite clear that these large channels are not caused by fracture of the weakened porous microstructure which has previously been noted in the reduction of hematite to magnetite. It is suggested that in that case the fracture is induced by the

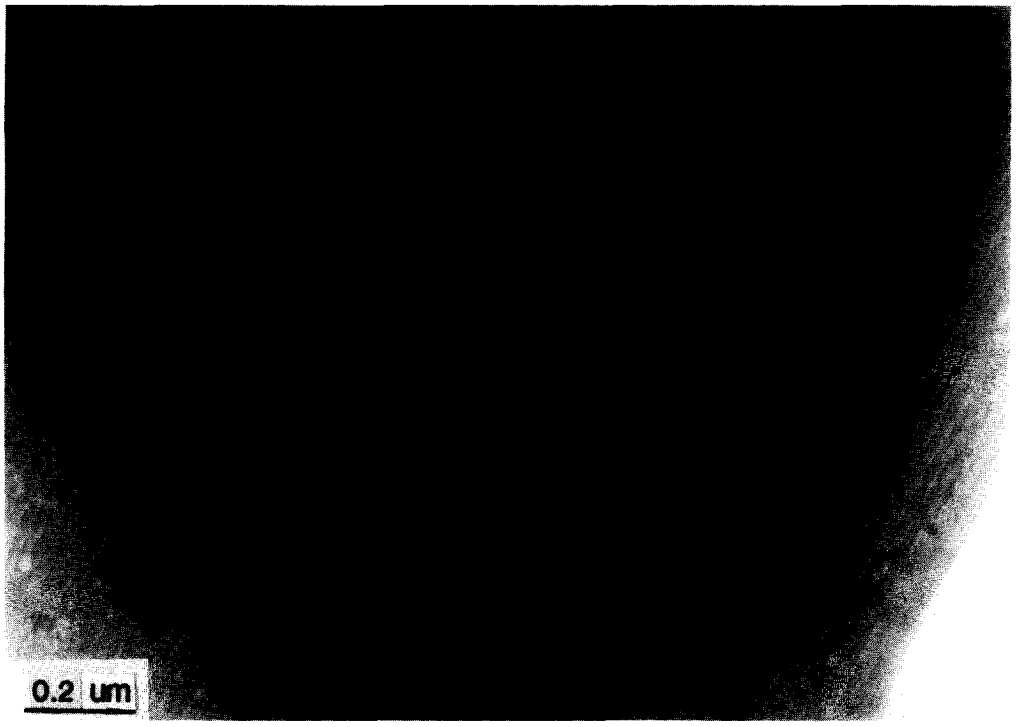

FIG. 15. HVEM *in situ* reduction of magnetite showing the preferential development of pores along the intersection of faults (seen most clearly at the arrowed locations) with the foil surface.

shear required to convert the hexagonal structure to a cubic one (*6, 21*) rather than by the specific volume change itself which is quite small (*6*). In the present case the much larger volume change is directly accommodated by the growth of the porous microstructure in which the only strain is that due to the epitaxy between the oxide and the metal.

Crystallographic Relationship between Magnetite and Iron

The orientation relationship found between magnetite and α-iron in the *in situ* studies and via examination of partially reoxidised prereduced material implies the existence of an epitaxial relationship between the two. An equivalent orientation relationship has been reported by Edstrom (*6*) between wüstite and iron. Given that the oxygen ions in wüstite occupy the same face-centered cubic sites as in magnetite this equivalence is not surprising. The same orientation relationship can be established indirectly from the epitaxial relationships reported for thin films of α-Fe on MgO and magnetite on MgO (*9, 28, 29*).

The Mechanism of Reduction and the Formation of Porous Iron

The cellular mechanism of reduction observed in this work produced a microstructure similar to that previously reported for the reduction of hematite to magnetite (*20, 21, 25*) and cobalt ferrite to metal (*22*) and may represent a general mechanism for reduction in which a net decrease in volume occurs during the reaction. Such a microstructural development provides direct gas access to the reaction front and short circuit diffusion paths for the ionic species which partition during reduction (Fig. 16).

The conditions under which a porous microstructure can develop are not clearly un-

derstood (*23*) and only limited microstructural evidence is available concerning the characteristics of pore size and reaction kinetics (*14, 2–24*). It has been suggested that the occurrence of a porous microstructure is temperature dependent (20–22, 25) and that decreasing the temperature decreases pore size and spacing: in the specific case of ammonia synthesis catalyst a small decrease has been reported as the reduction temperature decreases from 550 to 450°C (*14*). The effect of gas pressure is in general not documented although it should be noted that in the present work the *in situ* studies produced pore sizes of the order of 20 nm under a reduction pressure of only 30 Torr which is only slightly larger than the smallest pores, ~4–6 nm, observed in material reduced under commercial conditions (Figs. 5b and 11) of pressure ~150–350 atm. Porter and Swann (*21*) made qualitatively similar observations of a very weak pressure dependence of pore size for the hematite/magnetite reaction. Any model of the reduction reaction must be able to account for the effects of temperature and pressure on the reduction kinetics and the size of the pores produced. Figure 16 indicates schematically the migration paths of the species involved in the reduction reaction studied here producing a porous iron microstructure with alumina particles on the iron surfaces. In such a situation the

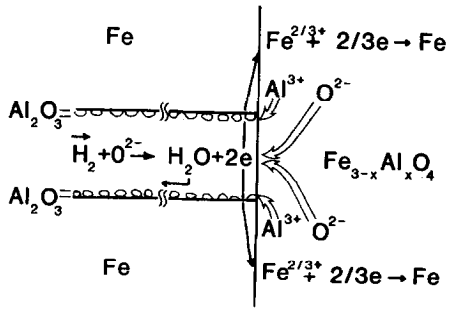

FIG. 16. A schematic diagram illustrating the chemical reactions associated with a single pore in the iron growing from the magnetite during reduction. The approximate paths followed by the various species are indicated.

kinetics of reduction may be controlled by a number of possible processes.

Al-Kahtany and Rao (*27*) have proposed the following for iron oxide reduction:

(i) hydrogen or water transfer between the gas phase and the solid;

(ii) the chemical reaction at the iron/oxide interface;

(iii) pore diffusion of hydrogen or water to and from the reaction front.

Additionally (iv) solid state diffusion of the ionic species through the oxide should also be considered. Baranski *et al.* (*14*) have successfully modelled the bulk reduction kinetics in the temperature range 450–550°C assuming (iii) to be rate limiting but incorporating into the model allowance for adsorption of water at the reaction interface. The agreement between theory and observation was extremely good. Al-Kahtany and Rao studied thin (89 μm) sections of Al free magnetite in the temperature range 234–620°C, thus approximating the conditions to those at the earliest stages of reduction of bulk material. Under these conditions they showed that pore diffusion was not rate limiting. The pore sizes developed were much larger (~3.6 μm) than those observed at the same temperature in the present work and that of Baranski *et al.* However, substitution of the present pore sizes into their equations indicates that in the thin foils studied in the million volt electron microscope gas transport will not be rate limiting. It is interesting to note, however, that the pore sizes observed in the *in situ* reduction are comparable to those obtained in bulk. This suggests that the pore size developed during reduction is not directly controlled by gas transport.

Obviously the gas transport rate must be sufficient to supply a free energy driving force per unit volume for reduction, at the reaction front, greater than the surface energy, per unit volume, of the porous iron produced.

The surface energy in the present case is ~0.5 kJ mol^{-1} which is very small in relation to the free energy driving force for reduc-

tion:

$$\Delta G = \Delta G^\circ + 3RT \log(P_{H_2O}/P_{H_2}) \text{ per mol Fe}$$
$$\Delta G^\circ \sim 1 \text{ kJ mol}^{-1}$$

This implies that there is no risk of a building up of water vapour at the reaction front to a point where a porous structure could not be sustained. At the initiation of reduction the partial pressure of water vapour can be very low indeed as it is rapidly swept away from the free iron surface in the flowing gas. Hence ΔG may rise to a very high value and an extremely fine pore structure could be supported. This would rapidly coarsen post reduction to reduce the surface energy per unit volume of the α-iron.

This phenomenon may be responsible for the mottling of the iron noted in the initial stages of *in situ* reduction. As the reaction front moves into the oxide the pore structure moves to the dynamic equilibrium value associated with steady state reduction. Al-Kahtany and Rao (*27*) associated this stage of reduction with mechanism (ii). Hayes and Grieveson (*23, 24*) suggest that the porous growth is controlled by the mobility of the reaction interface, while others (*20, 21, 24*) suggest that solid state ionic diffusion controls the process. A weak pressure dependence of pore size could reflect changes in point defect concentration, and hence diffusivity, with changes in hydrogen and oxygen activities in the gas phase (*32*). Pore size will increase with temperature as the ionic diffusivity increases and ions can move larger distances per unit time. Ionic diffusion is necessary since iron and oxygen must partition to the iron crystallites and pores, respectively, as the reaction proceeds (Fig. 16). Aluminium may thus be of considerable importance in this regard. It has been observed directly in this work that aluminium, initially in solution in the magnetite, diffuses out during reduction and resides on the reduced iron surfaces. Enrichment of the surface of the iron in the lighter elements has been deduced previously by indirect techniques (*1–3, 10*) and recently by scanning Auger electron microscopy (*26*). The pore sizes obtained, in the presence of this surface enrichment, are very much finer than those produced in iron itself (*27, 30*) as noted by Ertl and co-workers (*26*). It is tempting to interpret this as a direct consequence of aluminium diffusion across the reaction front representing the rate-limiting step. However, it is known (*1, 2*) that structural promoters, such as aluminium, hinder sintering: indeed the absence of sintering was directly observed in the *in situ* reduction experiments in the electron microscope reported in this work. Therefore the finer porosity observed may simply result from the inhibition of post reduction sintering which is rapid in the case of pure iron.

The present study has clearly shown that the aluminium is drawn from solid solution in the iron oxide rather than from the intergranular ferrite and glassy phases. Indeed the only element to redistribute from these regions is the highly mobile potassium (Fig. 13 and Table 1) which is well known to migrate rapidly over the iron surfaces. Other than this the only direct influence of the intergranular phases is to induce a locally much coarser porosity in the reduced state. After reduction small quantities of aluminium and calcium were detected (using X-ray energy dispersive analysis, Fig. 7) remaining within the iron crystallites. Transmission electron microscopy clearly shows that these are essentially free from defects. Hence the calcium and aluminium are necessarily present in solution in the iron and are not present as internal precipitates nor are they segregated at stacking faults in the iron as postulated previously on the basis of indirect measurements (*8, 11, 13, 31*). This confirms the suggestion of Ertl and co-workers (*26*) and implies that inhibition of sintering is due solely to the creation of the aluminium-rich surface layer on the iron.

CONCLUSIONS

1. *In situ* reduction in the HVEM repro-

duces microstructurally the commercial reduction product although the operating pressure is $\sim 10^3$ orders of magnitude lower.

2. The reduction reaction occurs via a cellular reaction producing a fine structure of crystalline iron and pores.

3. Pores develop preferentially from stacking faults in the magnetite which are associated with high calcium concentrations.

4. The iron nucleates epitaxially on the magnetite and forms crystals approximately 50 nm in size.

5. The elements present in the intercrystalline ferrite and glassy phases are essentially immobile during reduction with the exception of potassium which rapidly migrates over the reduced iron surfaces.

6. Aluminium, initially in solution in the oxide, partitions to the iron crystallite surfaces during reduction and inhibits sintering of the reduction product.

7. At 450°C the scale of the porosity may be controlled by the rate of partitioning of the aluminium to the iron surfaces.

REFERENCES

1. Bridger, G. W., and Snowden, C. B., "Catalyst Handbook." Wolfe Scientific, London, 1970.
2. Ozaki, A., and Aika, K., *in* "Catalyst Science and Technology" (J. R. Anderson and M. Boudart, Eds.), Vol. 2, Springer-Verlag, Berlin, 1981.
3. Chen, H. C., and Anderson, R. B., *J. Catal.* **28,** 161 (1973).
4. Dry, M. E., and Ferreira, L. C., *J. Catal.* **7,** 352 (1967).
5. Goldschmidt, H. J., *J. Iron Steel Inst.* **2,** 157 (1942).
6. Edstrom, J. O., *J. Iron Steel Inst.* **175,** 289 (1953).
7. Garbassi, F., Fagherazzi, G., and Calcaterra, M., *J. Catal.* **26,** 338 (1972).
8. Fagherazzi, G., Galante, F., Garbassi, F., and Pernicone, N., *J. Catal.* **26,** 344 (1972).
9. Gondo, Y., *J. Phys. Soc. Japan* **17,** 1129 (1962).
10. Dry, M. E., du Plessis, J. A. K., and Lauteritz, G. M., *J. Catal.* **6,** 194 (1966).
11. Topsøe, H., Dumesic, J. A., and Boudart, M., *J. Catal.* **28,** 477 (1973).
12. Brill, R., *J. Catal.* **19,** 236 (1970).
13. Pernicone, M., Fagherazzi, G., Galante, F., Garbassi, F., Lasserin, F., and Mattera, A., *in* "Proceedings, 5th International Congress on Catalysis, Palm Beach, 1972" (J. W. Hightower, Ed.), p. 1241. North Holland/American Elsevier, Amsterdam/New York, 1973.
14. Baranski, A., Lagan, M., Pattek, A., Reiser, A., Christiansen, L. J., and Topsøe, H., *in* "Preparation of Catalysts, II," (B. Delmon, P. Grange, P. Jacobs, and G. Poncelet, Eds.), p. 353. Elsevier, Amsterdam, 1979.
15. Reiser, A., and Baranski, A., *Appl. Catal.* **9,** 343 (1984).
16. Jensen, E. J., Topsøe, H., Sorensen, O., Krag, F., Candia, R., Clausen, B. S., and Mørup, S., *Scand. J. Metal.* **6,** 6 (1977).
17. Pattek-Janczyk, A., Hrynkiewicz, A. Z., Kraczka, J., and Kulgawczuk, D., *Appl. Catal.* **6,** 35 (1983).
18. Swann, P. R., "Electron Microscopy and Structure of Materials," p. 878. Univ. of California Press, Berkeley, 1972.
19. Swann, P. R., and Tighe, N. J., *Jernkontoret Ann.* **155,** 497 (1972).
20. Swann, P. R., and Tighe, N. J., *Metall. Trans. B* **8,** 479 (1977).
21. Porter, J. R., and Swann, P. R., *Iron and Steelmaking* **5,** 300 (1977).
22. Porter, J. R., and de Jonghe, L. C., *Metall. Trans. B* **12,** 299 (1981).
23. Hayes, P. C., and Grieveson, P., *Metall. Trans. B* **12,** 579 (1981).
24. Hayes, P. C., and Grieveson, P., *Metall. Trans. B* **12,** 319 (1981).
25. Brill-Edwards, H., and Samuel, R. L., *J. Iron Steel Inst.* **203,** 361 (1965).
26. Ertl, G., Prigg, D., Schoegl, R., and Weiss, M., *J. Catal.* **79,** 359 (1983).
27. Al-Kahtany, M. M., and Rao, Y. K., *Iron Steelmaking* **8,** 49 (1980).
28. Sato, H., Toth, R., and Astrue, R. W., *J. Appl. Phys.* **33,** 1113 (1962).
29. Takei, H., and Tatasu, S., *Jap. J. Appl. Phys.* **3,** 175 (1965).
30. Peters, C., Schafer, K., and Krabetz, R. L., *Elektrochem. Z.* **64,** 1194 (1960).
31. Ludwiczek, H. J., Preisinger, A., Fischer, A., Hosemann, R., Schonfeld, A., and Vogel, W., *J. Catal.* **51,** 326 (1978).
32. Birks, N., and Meier, G. H., "Introduction to High Temperature Oxidation of Metals," p. 75. Arnold, London, 1983.